Defence Science Journal, Vol. 70, No. 1, January 2020, pp. 3-9, DOI : 10.14429/dsj.70.14145

A Multi-segment Morphing System for a Micro Air Vehicle using Shape Memory Alloy Actuators

Kamalakannan G.M.[#,*], Giresh Kumar Singh[#], and C.M. Ananda[#]

[#]*CSIR-National Aerospace Laboratories, Bengaluru - 560 017, India*
[*]*Visveswaraya Technological University, Belagavi - 590 018, India*
[*]*E-mail: kannangm@nal.res.in*

ABSTRACT

A configurable multi-segment morphing system for a micro air vehicle (MAV) is presented in this study. One of the novelties is the development of an adaptive control allocation algorithm that provides fast, simultaneous and independent operation of four morphing segments using shape memory alloy (SMA) actuators. The SMA operation is time-staggered in microsecond resolution to ensure that only one SMA draws power from the MAV battery at a time. The other novelties are the in-flight measurement of morphing angle using dual flex-sensors and morphing of leading edges such that the 'morphing-line' is diagonal (45º) to the MAV's lateral axis. The system was implemented on an open source autopilot controller and operated using the MAV battery. It was ground-tested under propeller ON conditions and a droop rate of 35º/s and ability to track a 1 Hz sinusoidal variation of droop angle were realised.

Keywords: Multi-segment morphing; Adaptive control allocation; Leading edge drooping; Micro air vehicle; Time-staggered control; Drooping angle control

1. INTRODUCTION

The concept of morphing or shape changing of air vehicle precedes the Wright brother's first airplane[1]. Researchers have equivocally stated that an aircraft wing is an engineering compromise and morphing can reconfigure it to suit various flight phases or missions with increased efficiency[2]. Wing morphing to get improvement in aerodynamics can involve: planform morphing (span, sweep, and chord), Out-of-plane morphing (twist, dihedral/gull, and span-wise bending) and airfoil morphing (camber and thickness)[3]. It has the potential to increase the lift coefficient, aerodynamic efficiency, reduce drag and landing speed, increase resistance to stall[4], etc. Realising morphing features with benefits outweighing the penalties is a multi-disciplinary research challenge[5]. The complexity of these challenges increases in micro air vehicle (MAV), which are more sensitive to weight, space and energy demands[6].

Comparatively, camber morphing requires simpler changes in geometry and structure. Hence, they can provide significant aerodynamic improvements at lesser weight and energy penalties[7]. Camber morphing can be accomplished by drooping or extending the leading edge (LE) or trailing edge (TE)[8], deploying other control surfaces[9], changing the wing thickness[10], deflecting the wing skin[11] or their combinations[12]. Use of multiple small-scale shape-changing devices is more efficient and it also permits new morphing combinations.

Received : 15 February 2019, Revised : 03 June 2019
Accepted : 24 July 2019, Online published : 10 February 2020

1.1 Actuators for Morphing Wing MAV

Morphing requires compact and easy to operate actuator that has a high force to mass ratio, lower power consumption and good actuation speed. Electrically operated planar actuator such as the dielectric elastomer-'VHB 4910', gives very high strain (failure at 860 per cent) but low-stress (less than 0.3 MPa)[13]. Detail work for the design of such actuator for practical applications can be found in[14]. Shape memory polymers (SMP) have moderate strain levels of 50-100 per cent and stress levels of 2-10 MPa but have low actuation rates[15]. Servo actuators though widely used in MAV, occupy more space, weigh more than the SMA actuator system[16] and require gears, moving mechanical linkages and free space around them. Hence, all these actuators are not suitable for morphing multiple segments in MAV. Among various smart materials, Nickel-Titanium (Ni-Ti) SMA possess a higher force to mass ratio and caters to applications demanding higher recovery stress levels of 500 to 900 MPa and strain levels up to 5 per cent[17]. Further, they can be easily deployed and operated with a wide range of DC or AC unregulated low voltage supplies.

SMA actuator control methods described in literature use DC-DC converters, programmable power supply, load cell, laser interferometer, strain gauge[18], etc. All these approaches require more space, power and weight budget. Sensor-less control technique of SMA employs a current transducer or a burden resistor to calculate the SMA resistance and estimate its displacement[19,20]. This technique suffers from high noise, hysteresis, power drain, inaccuracy, lack of data during cooling

phase and computationally intensive artificial intelligence based methods[20].

The slow operating speed of SMA, particularly during cooling is also a limiting factor. The SMA actuation rate was increased up to 1 Hz by forced water-cooling for an oscillating hydrofoil application[21]. Similar actuation rates were obtained at 1.6 per cent strain by varying the current from a higher value to a safe value[22]. However, these methods need additional circuitry, system and energy. In another approach, for applications like safety release, high voltage (up to 125 V) pulses were used to get 3.6 per cent stroke on an SMA of diameter, 76 µm, in 40 ms time[23]. Increasing the SMA actuation speed using such high voltage may drastically reduce the life of the actuator.

Multiple SMA actuated morphing system for MAV, at less than 6.0 g per channel, with time-staggered control and typical droop rate of 4.4º/s, deactivation rate of 2.6º/s and control accuracy of ±0.5º was already reported[24]. The present work attempts to maximise the SMA actuation speed without compromising its life while tracking up to four different setpoint profiles simultaneously. It proposes high-speed switching of MAV battery supply to SMA-wire actuators through an adaptive control allocation algorithm that is built on a gain scheduled, PID control algorithm. It also presents an improved technique for measuring the degree of morphing or droop angle (DA).

The composition of the SMA actuator (manufactured at CSIR-NAL) used in this work is 44.5Ni-50.0Ti-5.5Cu at. %, (atomic percent) and its properties are available in[25,26]. The loads acting on the SMA wire due to the structural stiffness of the morphing segment (which also provides the restoring force to the SMA) and the aerodynamic forces have been modelled along with the SMA hysteresis effect[26]. Accordingly, the SMA wire of diameter 0.15 mm and length 180 mm was chosen[24]. In this application, the maximum SMA strain is 1.2 per cent and the stress is 300 MPa[26]. The SMA actuators are thermally insulated with a Teflon™ sleeve of 0.2 mm diameter to reduce the heat loss under the influence of propeller induced airflow.

2. LEADING EDGE DIAGONAL-MORPHING CONFIGURATION

The fixed wing MAV chosen for morphing has planar wings with Selig 4083 airfoil and inverse Zimmerman wingform. It has a wingspan of 300 mm and an all-up weight of 300 g. Earlier works on conventional aircraft have shown that LE Drooping has improved the C_L and the aerodynamic efficiency[27,28]. Based on this, at first, a MAV with its morphing line lying parallel to the lateral axis was built. The wind tunnel tests of this configuration have revealed marginal improvement in C_L occuring only at a higher angle of attack (AOA) without significant improvement in aerodynamic efficiency. Hence, as an alternative method, the morphing line was made to form 45º to the MAV lateral axis as shown in Fig. 1. This configuration has shown significant improvement in the aerodynamic efficiency for a wide range of AOA during wind tunnel tests. A brief explanation of the formation of morphing segments follows.

The line of morphing was first marked on the wing, symmetrically on either side and a cut was made along the line. The severed LE was reattached to the wing using four plastic hinge plates of size 20 mm by 25 mm that are embedded equally in the wing and the LE and bonded. A plastic bracket was also fixed at the middle of LE for attaching the SMA wire. With this arrangement, the LE deflects downwards when the SMA contracts due to Joule heating and temperature induced austenite phase transformation. The LE returns to the default position due to the stiffness of the plastic hinges, once the SMA cools and attains the martensitic phase. The extent of LE drooping was limited to six degrees, as the planar wing of MAV was already optimised. Further, maintaining higher DA calls for higher stress on the SMA actuator and more energy consumption.

In order to prove the four-segment morphing control concept, the elevons or the Trailing Edge (TE) part of the wing were also used as the morphing segments. Fig. 1 shows the four segment morphing MAV, along with the actuators, sensors and the associated electronics systems.

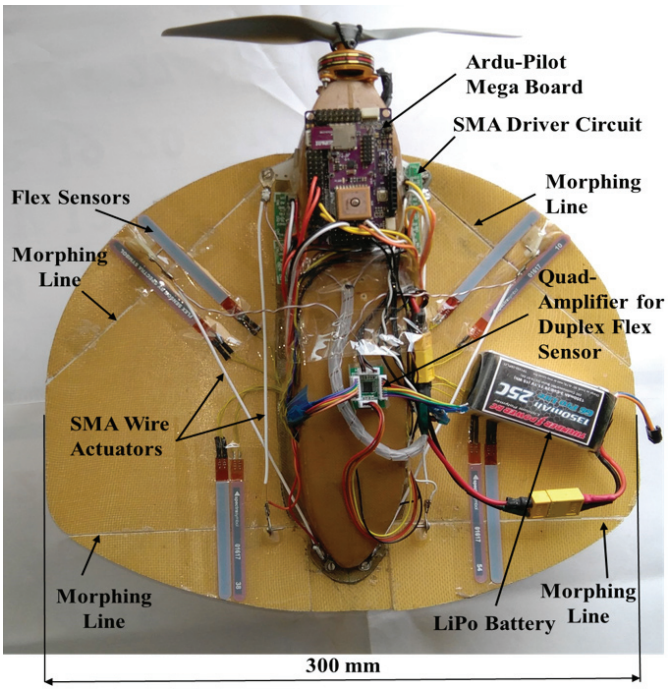

Figure 1. Four segment morphing MAV with dual flex sensors, SMA actuators, and electronics.

3. DROOP ANGLE MEASUREMENT

Droop angle is measured using flex sensors. A flex sensor's resistance increases as a function of flexing or bending and returns to its nominal value, once the bending force is removed. When bonded across the rigid wing and the flexible leading edge, its resistance increases with the degree of drooping. In order to improve the sensitivity and accuracy, two flex sensors each weighing ~0.3 g were used for each of the morphing segments as shown in Fig. 1. By connecting them at the opposite arms of the Wheatstone bridge, the differential output as a function of DA was substantially increased. A Quad-Operational amplifier, 'LM324' that operates on a unipolar power supply (+5 V DC) amplifies the differential output of four such bridges and feeds them to the autopilot. The circuit schematic is as shown in Fig. 2 and the analysis follows.

The Thevenin Voltage and resistance at point 'A' and 'B' indicated in Fig. 2 is,

$$V_{T-} = \frac{V_{ref} R}{R + R(1+\delta)} = \frac{V_{ref}}{2+\delta} \quad (1)$$

$$V_{T+} = \frac{V_{ref} R(1+\delta)}{R + R(1+\delta)} = \frac{V_{ref}(1+\delta)}{2+\delta} \quad (2)$$

$$R_{T+} = R_{T-} = R_T = \frac{R(1+\delta)}{2+\delta} \quad (3)$$

where, V_{ref} is the regulated excitation voltage of the bridge, δ denotes the change in flex resistance, i.e $R_{flex} = R(1+\delta)$, V_{T+}, V_{T-} and R_{T+} and R_{T-} are the Thevenin equivalent voltages and resistances respectively of the bridge circuit at the positive and negative input of the operational amplifier. Note that R_{T+} is equal to the parallel combination of R1 and R4 and R_{T-} is the parallel combination of R2 and R3. The modified output voltage, V_{OM}, due to the connection of duplex resistors at two opposite arms is obtained as,

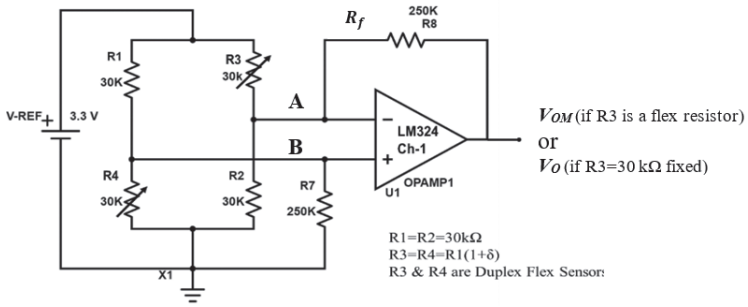

Figure 2. Wheatstone bridge amplifier with duplex flex sensors (R3 and R4) in two arms.

$$V_{OM} = (V_{T+} - V_{T-})\frac{R_f}{R_T} \quad (4)$$

Substituting for V_{T+}, V_{T-} and R_T in Eqn. (4), we get,

$$V_{OM} = V_{ref}\frac{\delta}{(1+\delta)}\frac{R_f}{R} \quad (5)$$

Similarly, the output voltage, V_o, with flex resistance in one arm and R3=30 kΩ fixed, can be determined as,

$$V_O = V_{ref}\frac{\delta}{(2+\delta)}\frac{R_f}{R} \quad (6)$$

Therefore,

$$\frac{V_{OM}}{V_O} = \frac{2+\delta}{1+\delta} \quad (7)$$

The Eqn. (7) shows that the modified circuit increases the output voltage, by two times for smaller values of δ and by 1.5 times for larger values (100%), thus increasing the sensitivity of DA measurement by the same ratio. The non-linearity between the DA and flex resistance was corrected in the program through the experimentally determined polynomial curve fitting parameters. The variations in the initial resistance of the flex sensor (due to temperature or otherwise) and the imbalance in the bridge circuit were compensated through the software based auto-nulling process.

4. CONTROL SYSTEM IMPLEMENTATION

The block schematic of the four-segment morphing system with SMA wire actuated LE and TE of the wing is as shown in Fig. 3. The SMA wires are connected to the MAV battery through a MOSFET, which is acting as a high-speed electronic switch. The Quad amplifier feeds the four DA signals to the analog input channels of the autopilot

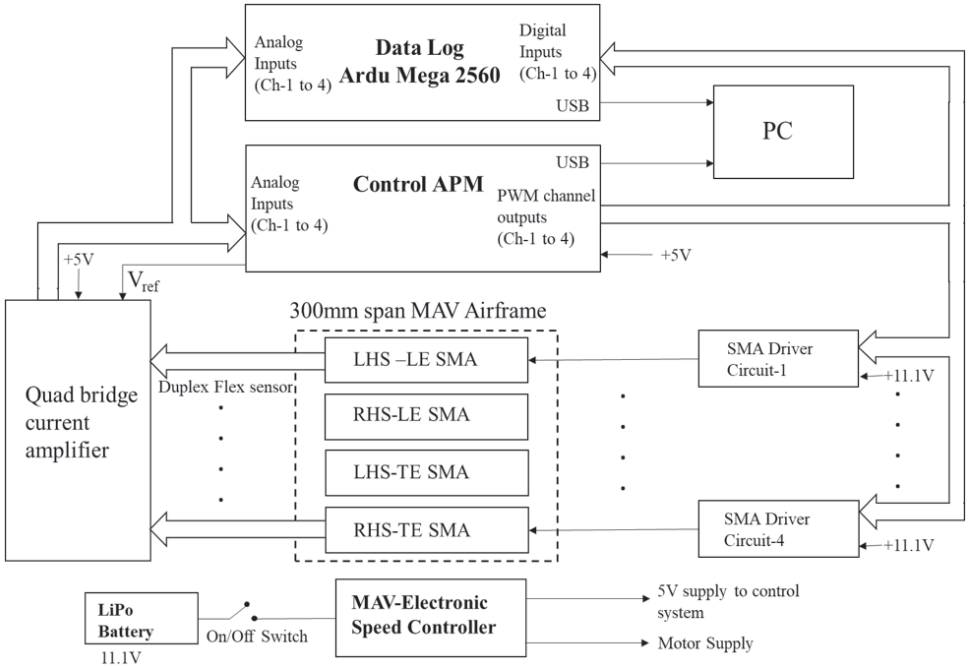

Figure 3. Block schematic of Multi-segment Morphing control system.

board ('Ardu Pilot Mega'-APM 2.5). A data logger board (Ardu Mega-2560), was used only during the experimentation phase for viewing all the control related data on the PC. It will be removed and all the electronics systems will be assembled inside the fuselage along with a wireless communication system during flight test.

The four morphing channels are controlled using pulses produced by APM that are time-staggered to ensure that at any instant of time only one SMA draws current from the battery. An adaptive control allocation algorithm (explained in section 4.1) dynamically varies these time durations. The control system was tuned using Ziegler-Nichols step response method to arrive at two sets of PID values: one for faster actuation and the other for reduced overshoot. A gain scheduler was coded to choose either of the two PID sets, depending on the error band.

4.1 The Concept of Adaptive Control Allocation

The control algorithm runs four PID control loops with independent parameters, such as, set DA, measured DA, PID gains, etc. and generates four control outputs (CO) of range 0 to 100%. In the previous work, the four COs were time-staggered to ensure that the MAV battery is not loaded by more than one SMA at a time[24]. Time staggering was realised by dividing the loop time (4 ms) into four equal parts (1 ms each) and sequentially allotting them to each channel, whether they use it or not. As the CO varies from 0 to 100%, the pulse on time (POT) of each channel varies from 0 to 1 ms continuously with a resolution of 1µs. Even if the CO of a channel is zero, the time allotted (1 ms) to it remains reserved and other channels cannot use this. Hence, the maximum duty cycle (the ratio of pulse on time to the total pulse duration) cannot exceed 25% or 0.25. In the present work, the concept of adaptive control allocation has been developed to overcome this drawback and substantially increase the rate of SMA actuation.

In a practical control situation, if one or more morphing channels are either not used or their power requirement is low, then their allotted Pulse On Time (POT) becomes free. The basic idea of adaptive control allocation algorithm is to allot this free time to the channel(s) that needs more power, thereby increasing the actuation rate. It computes the initial POT for every channel and limits it to double the nominal allocation (i.e. CO of 0-100%, now corresponds to 0-2 ms). If all the channels require more than 1 ms, then they all will be limited to 1 ms. If the POT of few channels is zero or less than the nominal (1 ms), then the excess time available will be proportionately allotted to the channels requiring more power. If the power required by all the channels is low, then the loop time is reduced from 4 ms to a minimum of 3 ms, to speed up the error correction process. This would result in a reduction of pulse duration and hence pulse frequency and pulse width modulation. Increase of POT to 2 ms and reduction of the pulse duration to 3 ms, results in an increased duty cycle of up to ~66.7% or 0.667. As the duty cycle is increased, faster actuation and overshoot occurs. To avoid the overshoot, a gain scheduler was implemented. The implementation details are as given in section 4.2.

4.2 Adaptive Control Allocation Algorithm

The executable code in APM has two functions, namely, 'setup' and 'loop'. The former is executed once, upon power ON and the latter is executed repeatedly. The 'setup' function is used to initialise four timers (16 bit), configure the APM input/output pins, enable timer overflow interrupts, initialise the timer's output compare registers, set the PC-communication parameters and initialise all the control variables, etc.

The 'loop' function executes the following tasks repeatedly:

(i) Get the instantaneous set DA (setpoint or SP) from user command or the programmed profile

(ii) Determine the actual DA (Process Variable or PV) from the DA signal by auto-nulling, averaging and applying the polynomial fit for non-linearity correction

(iii) Calculate the Control Output (CO) and POT using the following steps:
   (a) If the SP is zero or less, or if the DA is greater than the maximum limit, let the CO equals zero and go to step-4
   (b) If the absolute error is less than 'tolerance' (control accuracy), maintain CO and go to step-4
   (c) If the error (SP-PV) is greater than the threshold, apply PID set-1 (for rapid heating) else apply the PID set-2 (for regulation). Compute PID output and limit it to a range of 0 to 100%
   (d) POT: = CO/100 * *Max. Pulse width*

(iv) Carry out steps 1 to 3 for all the four morphing channels

(v) Let the total on time be the sum of POT of all the channels. If it is greater than the maximum pulse period (4 ms), then modify the additional-POT using the following logic, otherwise, go to step-6:
   (a) If a channel requires less than allotted pulse width (1000 µs), add the leftover time to *FT*, where, *FT* is the *Free time* available
   (b) If a channel requires more than 1000 µs, add the additional time required to *AT*, where, *AT* is the *Additional time* needed
   (c) Calculate, *Excess POT Factor (EPF)* as the ratio of total *FT* and *AT*
   (d) For every channel, if POT is greater than 1000 µs, then let:
   POT: = 1000 + (EPF * (POT-1000))

(vi) Store the POT of channel-1 as the on-time of timer-1; Store the sum of POT of ch-1&2 as the on-time of timer-2; Similarly, set the on-time for timer-3 and timer-4. Note that the timer-4's on-time will be the sum of all the POT. Set the total period of each timer as the sum of all the POT or the *minimum loop time*, whichever is higher. Enable a channel if its POT is greater than zero or else disable it

(vii) Initialise all the SMA actuator signal to zero and turn ON channel-1 alone, if it is enabled. Once Timer-1 interrupt occurs on completion of its on-time, turn OFF channel-1 and turn ON channel-2, if it is enabled. Perform similar operation for the outputs of Channels - 2 to 4, based on the interrupts from timer - 2 to 4

The above algorithm was coded and implemented as a part of the MAV autopilot software.

5. TESTS AND RESULTS

The unique concept of adaptive control allocation was explained as in section 4. The control system's performance was tested with propeller off and propeller running at full speed for different DA profiles. The set DA, actual DA and pulse width were logged for all the channels along with the process time.

First, the adaptive pulse width generation was tested through simulation by giving a fixed CO (in the code) to all the four channels and disconnecting the SMA power. This will give periodic and repetitive control signals to all the channels. These signals are displayed on a multi-channel digital storage oscilloscope and stored as an image file. By fixing the CO in such a way that few channels need less than the nominal time of 1000 µs, and few needs more, a situation of 'free time availability' and 'more power demand' is created. To test the algorithm for an example case, CO of ch-1 to ch-4 was fixed at 500 µs, 2000 µs, 1500 µs, and 500 µs respectively. This causes the total On-time to exceed 4000 µs. Therefore, the test condition at point-5 of the algorithm in section 4.1 becomes 'True' and tasks listed at 5.a to 5.d gets executed. Accordingly, the '*FT'* becomes 1000 µs (due to ch-1 & 4) and the '*AT'* becomes 1500 µs (due to ch-2 & 3). Therefore, the EPF, which is the ratio of '*FT'* and '*AT'* becomes 2/3. As per point 5.d of the algorithm, POT of ch-2 becomes 1667 µs and ch-3 becomes 1333 µs. The control signals generated by the algorithm and captured in this scope are as shown in Fig. 4(a). The pulse width of these signals matches the calculated values.

As an example test case of Control Outputs that would result in an increased Pulse Frequency, CO values for ch-1 to ch-4 were fixed in the code as 0 µs, 500 µs, 800 µs and 1000 µs respectively. Since the sum of all the POTs is 2300 µs, as per point no.6 of section 4.1, the pulse period becomes 3000 µs, which is the minimum loop time. This results in a variation of both Pulse Frequency and Pulse Width (PFPW). The actual signals captured for this example, are as shown in Fig. 4(b). They match the calculated values.

Having verified the control logic for various test cases in addition to the two critical ones explained above, the controller testing was continued for different types of set DA profiles. The controller was programmed to raise the DA as a step function from 0º to 6º and return to 0º, the moment the actual DA reaches the set value. The results are shown as a comparison of the set and actual DA in Fig. 4(c). The initial one-second duration was used to determine the auto-zero value of the flex sensor. When a step increase in DA is commanded, the SMA gets power but takes definite time to cross its austenite start temperature, contract and attain the set DA. Once the set DA is attained, the SMA power is cut-off and the cycle is repeated after the DA falls below 0.5º. For a step input, the time taken to reach 6º DA was 0.17 s, implying a droop rate of 35 º/s.

The ability of the control system to track a sinusoidal set profile of 1 Hz is as shown in Fig. 4(d). During actuation, there is a good match between the set and the actual DA. But, during cooling, the DA could not fall to 0° and it could reach a minimum of ~0.5°. The corresponding SMA pulse duty cycle variations are also plotted (green colour). The test was repeated with propeller running at its full-speed and producing a wind velocity of 8.6 m/s (measured through an anemometer). The results are as shown in Fig. 4(e). Here, due to the propeller induced wind flow, and higher heat losses, a slight delay in

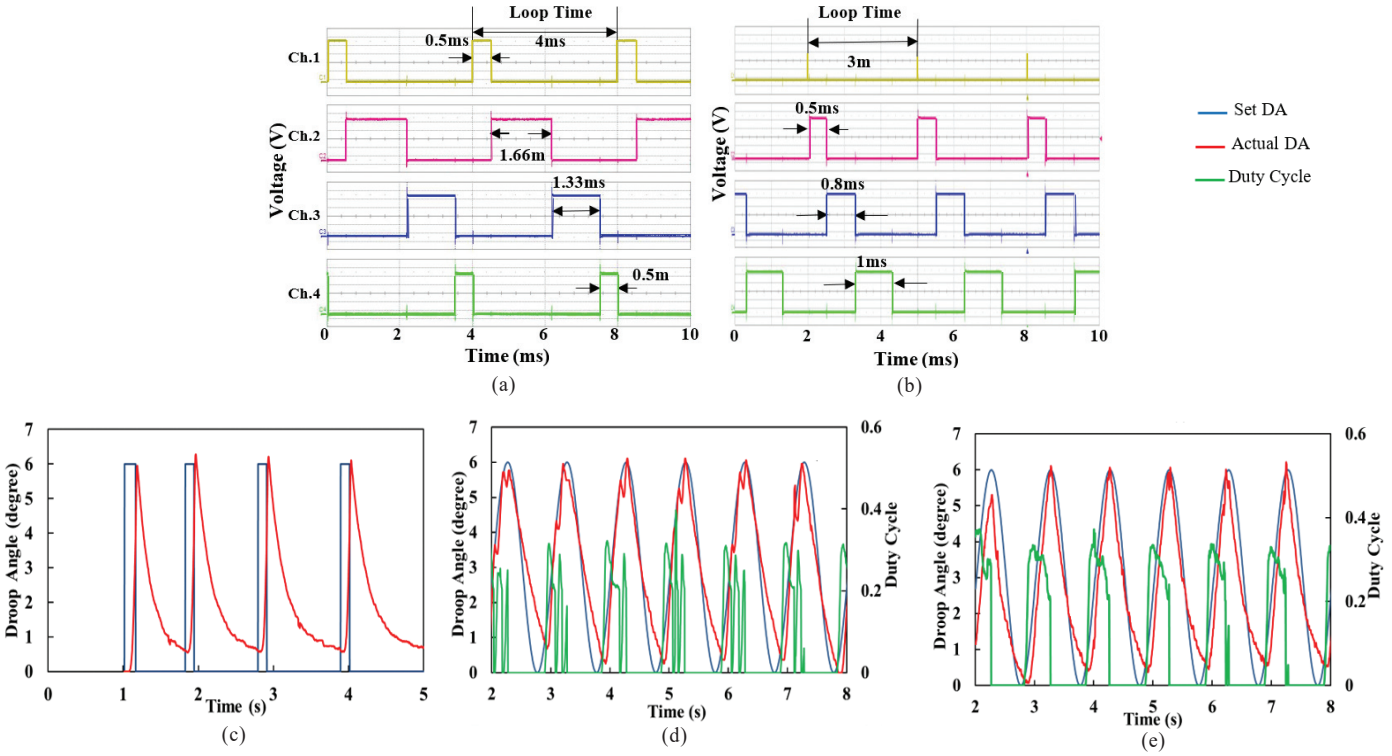

Figure 4. Performance of Adaptive control allocation system for high-speed SMA actuation: (a) Unused time of Ch- 1&3 allotted to Ch-2, (b) Unused time of Ch- 1 has reduced the loop time, (c) Set and actual DA profile for step input, (d) Sinusoidal DA control with propeller OFF, and (e) Sinusoidal DA control with propeller at full speed.

tracking the positive going cycle was observed. The power consumed, seen from the area of duty cycle has gone up. This is expected to have increased the core temperature of the SMA wire. Hence, the DA during cooling, is still slightly above 0°. The tracking performance has also shown improvement, as the tuning was optimised for propeller ON condition. The deactivation rate of DA from 6 º to 1º was 9.2º/s. The average energy consumption for sinusoidal profile tracking with propeller running at maximum speed was 1.12 J (~5.6% increase). The maximum value of duty cycle was limited to 0.66 to enable operation of other morphing segments and to avoid faster heating of SMA wire.

6. CONCLUSIONS AND FUTURE WORKS

A flight-capable, SMA actuated, four segment morphing MAV, where the morphing line of the leading edge is diagonal (45º) to the lateral axis was presented. The morphing angle measurement sensitivity was increased up to two-fold, using dual flex sensors, that form two unknown resistances of the Wheatstone bridge. A four-channel, Adaptive Control Allocation algorithm, built upon a time-staggered, gain-scheduled and PID based PFPW modulator was presented. The system was realised using an open source autopilot at an additional weight of 6-g per morphing segment. The program was validated for control signal generation using several test cases and two critical ones are presented.

The ability of the control system to closely track a 1-Hz sinusoidal DA profile, both under propeller off and full speed running conditions are presented. During this tracking, the algorithm has limited the duty cycle to 66.7%, in order to provide power to other morphing segments. The average increase in energy consumption due to maximum wind flow over the insulated SMA actuator while tracking a 1Hz sinusoidal DA profile was ~ 5.6%. This algorithm has resulted in a substantial increase in SMA actuation speed. The rate of actuation for a step change in DA was increased to 35º/s and the rate of deactivation to 9.2º/s under MAV-propeller running conditions.

Since the system provides four simultaneously morphing segments, a variety of morphing configuration can be explored from an aerodynamic point of view. The ability to actuate multiple SMA actuated segments, at relatively high speed while limiting the instantaneous current to that drawn by one segment is advantageous for number of battery operated applications. Weight of the control system will be further reduced by using light-weight PCB, connecting leads and connectors. An autonomous algorithm can be developed to decide on the degree of morphing depending on the flight conditions and the flight mission. Extensive wind tunnel tests, flight trials, tests under different environmental conditions and coordinated morphing to realise desired pitch and roll control rates etc. are due.

REFERENCES

1. Weisshaar, T.A. Morphing aircraft systems: Historical perspectives and future challenges. *J. Aircr.,* 2012, **50**(2), 337-353. doi: 10.2514/1.C031456
2. Barbarino, S.; Bilgen, O.; Ajaj, R.M.; Friswell, M.I. & Inman, D.J. A review of morphing aircraft. *J. Intell. Mater. Syst. Struct.,* 2011, **22**(9), 823-877. doi: 10.1177/1045389X11414084
3. Sofla, A.Y.N.; Meguid, S.A.; Tan, K.T. & Yeo, W.K. Shape morphing of aircraft wing: Status and challenges. *Mater. Des.,* 2009, **31**(3), 1284-1292. doi:10.1016/j.matdes.2009.09.011
4. Bowman, J.; Sanders, B.; Cannon, B.; Kudva, J.; Joshi, S. & Weisshaar, T. Development of next generation morphing aircraft structures. *In* Proceedings of the 48th AIAA/ASME/ASCE/AHS/ASC Structures, Structural Dynamics, and Materials Conference 2007. doi: 10.2514/6.2007-1730
5. Wlezien, R. W.; Homer, G. C.; McGowan, A. R.; Padula, S. L.; Scott, M. A.; Silcox, R. J. & Simpson, J. O. The aircraft morphing program. *In* Proceedings of the 39th AIAA/ASME/ASCE/ AHS/ASC Structures, Structural Dynamics, and Materials Conference and Exhibit 1998. https:// ntrs.nasa.gov/archive/nasa/casi.ntrs.nasa.gov/19980053567.pdf (Accessed on 15 July 2019).
6. Petricca, L.; Ohlckers, P. & Grinde, C. Micro- and nano-air vehicles: State of the art. *Int. J. Aerosp. Eng*., **2011**(Apr.), 1-17. doi:10.1155/2011/214549
7. Valasek, J. Morphing aerospace vehicles and structures. John Wiley & Sons, 2012. 46-48, 53 p. ISBN: 978-0-470-97286-1
8. Kudva, J.N. Overview of the DARPA smart wing project. *J. Intell. Mater. Syst. Str.,* 2004, **15**(4), 261-267. doi: 10.1177/1045389X04042796
9. Jayasankar S.; Kumar, P. Senthil; Varughese, B.; Ramanaiah, B.; Vishwanath, S.; Ramachandra, H.V. & Dayananda, G. N. Smart aerodynamic surface for a typical military aircraft using shape memory elements. *J. Aircraft,* 2011, **48**(6), 1968-1977. doi: 10.2514/1.C031391
10. Abdullah, E.J.; Bil, C. & Watkins, S. Application of smart materials for adaptive airfoil control. AIAA 2009-1359, 2009. doi 10.2514/6.2009-1359
11. Popov, A.V.; Grigorie, T.L.; Botez, R.M.; Mébarki, Y. & Mamou, M. Modeling and testing of a morphing wing in open-loop architecture. *J. Aircraft,* 2010**, 47**(3), 917-923. doi: 10.2514/1.46480
12. Smith, K.; Butt, J.; Von Spakovsky, M.R. & Moorhouse, D. A study of the benefits of using morphing wing technology in fighter aircraft systems. *In* the Proceedings of 39th AIAA Thermophysics Conference 2007: doi: 10.2514/6.2007-4616
13. Bozlar, Michael; Punckt, Christian; Korkut, Sibel; Zhu, Jian; Foo, Choon Chiang; Suo, Zhigang & Aksay, Ilhan A. Dielectric elastomer actuators with elastomeric electrodes. *Appl. Phys. Lett.,* 2012, **101**(9), 91907. doi: 10.1063/1.4748114
14. Sahu, R.K.; Saini, A.; Ahmad, D.; Patra, K. & Szpunar, J. Estimation and validation of maxwell stress of planar dielectric elastomer actuators. *J. Mech. Sci. Technol.,* 2016, **30**(1), 429-436.

doi: 10.1007/s12206-015-1247-y
15. Liu, Y.; Lv, H.; Lan, X.; Leng, J. & Du, S. Review of electro-active shape-memory polymer composite. *Compos. Sci. Technol.,* 2008, **69**, 2064-2068. doi:10.1016/j.compscitech.2008.08.016
16. Guglieri G. & Sartori, D. Experimental characterization of actuators for micro air vehicles. *Int. J. Micro Air Veh.,* 2011, **3**(2), 49-59. doi: 10.1260/1756-8293.3.2.49
17. Huang, W. On the selection of shape memory alloys for actuators. *Mat. Des.,* 2002**, 23**(1) 11-19. doi: 10.1016/S0261-3069(01)00039-5
18. Mohd Jani, J.; Leary, M. & Subic, A. Designing shape memory alloy linear actuators: A review. *J. Intell. Mat. Syst. Str.,* 2017, **28**(13) 1699-1718. doi: 10.1177/1045389X16679296
19. Ma, N.; Song, G. & Lee, H. J. Position control of shape memory alloy actuators with internal electrical resistance feedback using neural networks. *Smart Mat. Str.,* 2004**, 13**(4), 777-783. doi:10.1088/0964-1726/13/4/015
20. Asua, E.; Feutchwanger, J.; Garcia-Arribas, J. & Etxebarria, V. Sensorless control of SMA-based actuators using neural networks. *J. Intell. Mat. Syst. Str.,* 2010**, 21**(18), 1809-1818. doi: 10.1177/1045389X10388965
21. Rediniotis, O.K.; Wilson, L.N.; Lagoudas, D.C. & Khan, M.M. Development of a shape-memory-alloy actuated biomimetic hydrofoil. *J. Intell. Mat. Syst. Str.,* 2002, **13**, 35-49. doi:10.1177/1045389X02013001534
22. Featherstone, R. & Teh, Y. H. Improving the speed of shape memory alloy actuators by faster electrical heating. *In* Experimental robotics IX, Springer, 2006, 67-76. doi: 10.1007/11552246_7
23. Motzki, P.; Gorges, T.; Kappel, M.; Schmidt, M.; Rizzello, G. & Seelecke, S. High-speed and high-efficiency shape memory alloy actuation. *Smart Mat. Str.,* 2018, **27**(7) 075047, Jul. doi: 10.1088/1361-665X/aac9e1
24. Kamalakannan, G.M.; Gireesh Kumar Singh & Ananda, C.M. Versatile control of multiple morphing surfaces of micro air vehicle with reduced weight and optimized power consumption. *In* Third International Conference on circuits, control, communication and computing, 2018. doi: 10.1109/CIMCA.2018.8739704
25. Saikrishna, C.N.; Ramaiah, K.V. & Bhaumik, S.K. Effects of thermo-mechanical cycling on the strain response of Ni-Ti-Cu shape memory alloy wire actuator. *Mater. Sci. Eng. A*, 2006, **428**(1-2), 217-224. doi:10.1016/j.msea.2006.05.008
26. Kamalakannan, G.M.; Gireesh Kumar Singh & Ananda, C.M. Influence of thermal insulation and wind velocity on the SMA actuator for morphing applications. *J. Mech. Sci. Technol.*, 2019, **33**(9), 4459-4468. doi: 10.1007/s12206-019-0842-8
27. Monner, H.; Kintscher, M.; Lorkowski, T. & Storm, S. Design of a smart droop nose as leading edge high lift system for transportation aircrafts. *In* Proceedings of 50th AIAA/ASME/ASCE/AHS/ ASC Structures, Structural Dynamics, and Materials Conference 2009: doi:10.2514/6.2009-2128
28. Jayasankar, S.; Dayananda, G.N.; Varughese, B. & Senthil Kumar, P. SMA based adaptive concept on wings of large civil aircraft. *In* Symposium on Applied Aerodynamics and Design of Aerospace Vehicle (SAROD-2009), 2009. https://nal-ir.nal.res.in/9622/1/sarod2009_RTA_LE.pdf [Accessed on 15 July 2019].

ACKNOWLEDGEMENTS

The authors wish to thank Mr Jitendra J. Jadhav, Director, CSIR-NAL for his support and Dr G.N. Dayananda, Head, CSMST for suggesting the drooping concept. The authors also thank, Mr P. Arun, Mr K. Mohan Kumar, Mr D. Thulasi durai, Ms P. Nandini, Ms S. Navaneetha, and Mr K. Ramesha of CSMST, NAL for their support. Authors thankfully acknowledge the NPMASS, DRDO, India for funding the initial phase of this work.

CONTRIBUTORS

Mr G.M. Kamalakannan has MTech in Electronics Engineering. from VTU where he his currently pursuing PhD. He is currently a Senior Principal Scientist at CSMST. He has experience in the design, development and commercialisation of electronics, control and instrumentation systems and application software for aerospace composites process equipment, which include aerospace grade autoclave, multi zone hot bonder, automated resin infusion system. He has also lead a NPMASS project on morphing wing micro air vehicle.
He has conceived, designed, developed and tested the multi-segment morphing MAV with adaptive control allocation algorithm.

Dr Giresh Kumar Singh has BTech and MTech (Aerospace Engg.) and PhD (Electrical Engg.) from IIT-Kanpur. He is working as a Senior Principal Scientist in the Flight Mechanics & Control Division of CSIR-NAL. He has been involved in the design, development, and testing of flight control laws for civil and military manned aircraft as well as unmanned aerial vehicles for civilian and strategic applications. His Research Interest include: Flight dynamics of aerial vehicles, design of flight control algorithms and optimisation.
He has guided the research works on controls part of this paper.

Dr Ananda C.M. did his PhD in embedded avionics. He is working as a Chief Scientist and Head of Aerospace Electronics and Systems Division of CSIR-NAL. He has to his credit number of awards for excellent project execution of various projects, NAL Technology shield award and many more. He has 9 journal publications and 28 conference publications along with one book chapter.
He has guided the research work on electronics part of this paper.